Boott, C., Leitao, E., Hayward, D., Laine, R., Mahou, P., Guerin, G., Winnik, M., Richardson, R., Kaminski, C., Whittell, G., & Manners, I. (2018). Probing the Growth Kinetics for the Formation of Uniform 1D Block Copolymer Nanoparticles by Living Crystallization-Driven Self-Assembly. *ACS Nano*, *12*(9), 8920-8933. https://doi.org/10.1021/acsnano.8b01353

Probing the Growth Kinetics for the Formation of Uniform 1D Block Copolymer Nanoparticles by Living Crystallization-Driven Self-Assembly

Charlotte E. Boott,[†,ϕ] Erin M. Leitao,[†,ϕ,ϒ] Dominic W. Hayward, [†] Romain F. Laine,[§] Pierre Mahou,[§] Gerald Guerin,[ψ] Mitchell A. Winnik,[ψ] Robert M. Richardson,[‡,*] Clemens F. Kaminski,[§,*] George R. Whittell, [†,*] and Ian Manners[†,*]

[†]*School of Chemistry, University of Bristol, Cantock's Close, Bristol, BS8 1TS, U.K.*

[‡]*School of Physics, University of Bristol, Tyndall Avenue, Bristol, BS8 1TL, U.K.*

[§]*Department of Chemical Engineering and Biotechnology, University of Cambridge, Philippa Fawcett Drive, Cambridge, CB3 0AS, U.K.*

[ψ] *Chemistry Department, University of Toronto, 80 St. George Street, Toronto, M5S 3H6, Canada*

[ϒ] *School of Chemical Sciences, University of Auckland, 23 Symonds Street, Auckland, 1010, New Zealand*

Please address correspondence to robert.richardson@bristol.ac.uk, g.whittell@bristol.ac.uk, cfk23@cam.ac.uk and ian.manners@bristol.ac.uk

[ϕ]These authors contributed equally

Abstract

Living crystallization-driven self-assembly (CDSA) is a seeded growth method for crystallizable block copolymers (BCPs) and related amphiphiles in solution and has recently emerged as a highly promising and versatile route to uniform core-shell nanoparticles (micelles) with control of dimensions and architecture. However, the factors that influence the rate of nanoparticle growth have not been systematically studied. Using transmission electron microscopy (TEM), small- and wide-angle X-ray scattering (SAXS and WAXS), together with the super-resolution fluorescence microscopy techniques, we have investigated the kinetics of the seeded growth of poly(ferrocenyldimethylsilane)-*b*-(polydimethylsiloxane) (PFS-*b*-PDMS), as a model living CDSA system for those employing, for example, crystallizable emissive and biocompatible polymers. By

altering various self-assembly parameters including concentration, temperature, solvent, and BCP composition our results have established that the time taken to prepare fiber-like micelles *via* the living CDSA method can be reduced by decreasing temperature, by employing solvents that are poorer for the crystallizable PFS core-forming block, and by increasing the length of the PFS core-forming block. These results are of general importance for the future optimization of a wide variety of living CDSA systems. Our studies also demonstrate that the growth kinetics for living CDSA do not exhibit the first order dependence of growth rate on unimer concentration anticipated by analogy with living covalent polymerizations of molecular monomers. This difference may be caused by the combined influence of chain conformational effects of the BCP on addition to the seed termini, and chain length dispersity.

Keywords: block copolymers, self-assembly, nanofibers, reaction kinetics, laser scanning confocal microscopy.

A key scientific challenge of widespread current interest involves the creation of well-defined functional materials based on soft matter that exist on a length-scale of nanometers to microns.[1–5] One key strategy employed to achieve this goal is the solution processing of block copolymers (BCPs) with amorphous core-forming segments, which produces core-shell nanoparticles (micelles) with a range of morphologies and functionalities.[6,7] This has resulted in a variety of actual and potential applications from drug delivery to composite reinforcement.[8–11] Nevertheless, a major problem in this field is the limited ability to create uniform samples of micellar nanoparticles with predictable and anisotropic shape, tunable dimensions, and controllable spatially-confined core and/or corona chemistries.

The solution self-assembly of BCPs with a crystallizable core-forming block has recently emerged as a powerful route to core-shell nanoparticles with high levels of precision and control. Upon addition of a selective solvent for the corona-forming block to a molecularly dissolved BCP (unimer), both crystallization of the core-forming block and amphiphilicity influence micelle formation, with low curvature morphologies, such as cylinders and platelets, normally being favoured.

This process has now been studied for a wide range of BCPs with different crystallizable core-forming segments and has been termed crystallization-driven self-assembly (CDSA).[12–35]

Length control can be achieved using a CDSA approach through the application of seeded growth[36] techniques to produce low dispersity micelles. For example, previous work has shown that the exposed crystal faces at the termini of pre-existing cylindrical micelles with a crystalline poly(ferrocenyldimethylsilane) (PFS)[37] core remain active to further growth *via* epitaxy.[38] This technique can then be used to prepare monodisperse micelles of controlled length by the addition of a known amount of unimer to a colloidal solution of small crystallite seeds, generated by the sonication of multimicron long cylindrical micelles (Scheme 1).[36] The control of length through variation of the unimer-to-seed ratio can be considered to be analogous to molecular weight control in a living covalent chain growth polymerization, and the process has thus been termed living CDSA. Using this seeded growth approach, the sequential addition of BCPs with a common crystallizable core-forming block,[38] or different core blocks with a small lattice mismatch,[39] results in the formation of a range of multicompartment block comicelles with nanosegregated functionality.[40,41] A variety of BCPs with different crystallizable core-forming blocks has been shown to undergo living CDSA[32,37,39,42–44] and the process has been extended to amphiphiles that form supramolecular polymers.[45–56] For the BCPs, those with a PFS core-forming block have been the most widely studied to date. Living CDSA of PFS BCPs has recently been shown to be scalable[57] and to enable the preparation of a wide range of BCP nanoparticles, including 2D platelets,[58,59] non-centrosymmetric[60] and branched cylinders[61] and hierarchical structures, such as supermicelles[62,63] and superlattices.[64] Furthermore, a key feature of the resulting crystalline BCP assemblies is that a high barrier exists to unimer exchange between micelles at near ambient temperatures, which prevents equilibration, and the consequential loss of uniformity and complexity. PFS BCP-based nanoparticles also have advantages for many studies as staining is unnecessary for TEM analysis, as a result of the electron-dense Fe-rich PFS core and coronal derivatization (*e.g.* for functionalization by fluorescent dyes) is synthetically well-developed.[37]

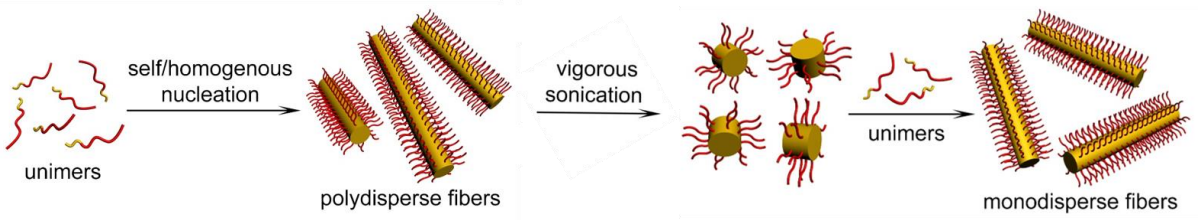

Scheme 1: Schematic representation of the preparation of monodisperse cylindrical micelles *via* seeded growth living CDSA.

Although many studies have now demonstrated the high levels of control possible using living CDSA, and that the epitaxial nature of the seeded growth process has been established for the cases of both 1D and 2D assemblies,[59,65–67] the factors that influence the kinetics are virtually unexplored. In a recent study we analyzed the formation of cylindrical micelles *via* the seeded growth of PFS-based linear and brush BCPs with chemically similar structures but different degrees of coronal steric bulk.[41] After addition of the BCPs to pre-existing seeds, the lengths of the fiber-like micelles were monitored as a function of time using transmission electron microscopy (TEM). It was found that the growth rates were substantially reduced by increasing steric bulk of the corona-forming block.

In this paper we report the use of TEM to monitor the growth of different PFS BCPs under a variety of conditions in order to obtain key fundamental information on the growth process. These methods are augmented by super-resolution fluorescence microscopy (SRFM) techniques, which are able to image individual nanoparticles in solution. In recent years, SRFM techniques such as structured illumination microscopy (SIM),[68,69] stimulated emission depletion microscopy (STED)[70–72] and single molecule localization microscopy (SMLM)[70,73–77] have emerged as impressive methods with which to visualize biological structures and their growth by nucleation-elongation processes.[78] For example, the formation of amyloid fibers has been studied in cells[79,80] and aqueous solution[81,82] using super-resolution techniques and a two-colour SMLM approach has been used to elucidate the growth kinetics of individual fibrils *in vitro*.[78,83,84] Furthermore, in recent work, SMLM has been used to observe dynamic exchange mechanism of supramolecular polymeric fibers, providing examples of the utility of these techniques to study non-covalent polymerizations.[85,86] We have also recently

demonstrated the use of STED and two-colour SMLM to image PFS-based BCP micelles in organic media, which demonstrated that the length data obtained by TEM analysis on dried samples is representative of the micelles in their native environment.[87] Based on these considerations, as complementary experiments to TEM, the SRFM techniques, STED and two-colour SMLM were employed to study the growth by living CDSA in solution. In addition, our micelle growth data were fitted to kinetic models, which enabled rate constants to be extracted quantitatively and detailed information on the living CDSA growth process to be obtained.

Results

Monitoring the growth of PFS_{63}-*b*-$PDMS_{513}$ one-dimensional micelles by TEM

In a typical living CDSA experiment, a PFS_{63}-*b*-$PDMS_{513}$[88] [PDMS = polydimethylsiloxane, subscripts indicate the number average degree of polymerization (DP_n)] unimer solution in THF was added to a solution of crystallite seed micelles, prepared by sonication of longer cylindrical micelles, in a selective solvent for the corona-forming block. A range of parameters was subsequently varied including concentration, temperature, selective solvent and percentage common solvent, and BCP composition. To monitor the effect of each of these parameters on the growth of PFS_{63}-*b*-$PDMS_{513}$ BCP micelles, aliquots were taken from the reaction mixtures at set time points, placed on carbon-coated copper grids and analyzed by TEM. This enabled the micelle length at different time points throughout the growth process to be determined.

The crystalline core structure of PFS BCP micelles

The key feature of PFS-based BCP micelles from the perspective of living CDSA is the crystalline PFS core. Previous studies using wide-angle X-ray scattering (WAXS) of PI_{637}-*b*-PFS_{53} cylindrical micelles (PI = polyisoprene) have shown that the PFS chains extend perpendicular to the long axis of the micelle and pack with pseudo hexagonal symmetry.[65] Further studies involving micelles from a range of different PFS-containing BCPs suggest that the core cross-section can be either rectangular, elliptical or near circular, depending on the degree of polymerization of the core-forming block.[89,90] This change in core structure results from different numbers of chain-folds within

the cross-sectional area, while the spacing between chains remains the same. The majority of experiments discussed herein involve the use of the same PFS-containing BCP, namely, PFS_{63}-*b*-$PDMS_{513}$. This enabled us to investigate whether the factors that influence the micelle growth rate also had a simultaneous effect on the micelle cross-section. For the BCP used in these experiments, both short (L_n = 92 nm, PDI = L_w / L_n = 1.07, where L_n and L_w represent the number/weight average contour length,) and long (L_n = 1757 nm, PDI = 1.01) low length dispersity micelles were prepared by seeded growth, and the micelle structures were analyzed by small- and wide-angle X-ray scattering (SAXS and WAXS) and TEM (Figure S1). The SAXS data for both sets of micelles was best fitted by a model for infinite rigid rods with a rectangular cross-section. This afforded core dimensions of 8.6 ± 1.8 x 7.6 ± 2.8 nm and 9.4 ± 0.8 x 7.4 ± 0.1 nm for the short and long micelles, respectively (Table S1). The model also incorporated a corona extending from the narrow side of the core, which refined as 18.5 ± 3.4 nm for the short micelles and 17.4 ± 0.5 nm for the long examples. It is noteworthy that the polydispersity in the wide dimension of the core was much larger than in the other, which may suggest a deviation from a purely rectangular cross-section. Analysis by high-resolution TEM revealed number average contour widths, W_n, of 11 nm for both samples, which we view to predominantly reflect the core width. These data are therefore in reasonable agreement with wider core dimension as determined by SAXS, and together demonstrate that the micellar structure does not change with contour length. The linear aggregation numbers (*i.e.* the number of PFS BCP molecules per unit length) were 3.5 ± 1.5 and 3.7 ± 0.3 chains/nm for the short and long micelles, respectively (see Supporting Information page 4), which are the same within error.[91]

Varying the growth conditions for PFS_{63}-*b*-$PDMS_{513}$ one-dimensional micelles

Effect of initial unimer concentration

The overall length of fiber-like micelles formed in living CDSA seeded growth experiments is proportional to the unimer-to-seed ratio. This is analogous to living covalent polymerizations in which the chain length is dependent on the ratio of monomer to initiator. It was therefore of interest to investigate whether this analogy also applied to the reaction kinetics. In a living covalent polymerization the reaction is first order in both monomer and initiator concentrations,[92] and this

would translate to the reaction being first order in both unimer, [*U*], and seed, [*S*], concentrations for living CDSA. As the latter remains constant during the course of the reaction, and initiation occurs from both ends of the seed, [*S*] should be substituted by $2[S]_0$ (the concentration at $t = 0$) in the differential form of the rate equation (Eq. 1).

$$\frac{d[U]}{dt} = -k[U]2[S]_0 \qquad \text{Eq. 1}$$

Integrating Eq. 1 then affords an expression for the concentration of unimer as a function of time, [*U*(*t*)], in terms of the initial concentrations (Eq. 2).

$$[U(t)] = [U]_0 e^{-2k[S]_0 t} \quad \text{Eq. 2}$$

Determining the concentrations of micelle and unimeric BCP in solution, however, is problematic. We therefore chose to monitor the reaction kinetics by determining the average length, *L*(*t*), of the individual micelles formed, which could be measured microscopically. The total length grown over all micelles, $L_{tot}(t)$, is related to the concentrations of unimer, [*U*(*t*)] and U_0, the volume of solution, *V*, and the linear aggregation number (number of BCP molecules per unit length), $N_{agg/L}$ (Eq. 3). We have shown (*vide supra*) that the latter is constant with micelle length, under the growth conditions used.

$$[U(t)] = [U]_0 - \frac{L_{tot}(t)N_{agg/L}}{N_A V} \qquad \text{Eq. 3}$$

Rearranging Eq. 3 to make $L_{tot}(t)$ the subject and dividing by the number of micelles, which for a living process equals the number of seeds, N_{seed}, then affords an expression for the length grown $L_{grown}(t)$ for each micelle (Eq. 4).

$$L_{grown}(t) = \frac{1}{N_{seed}} \frac{N_A V}{N_{agg/L}} [U]_0 \left(1 - e^{-2k[S]_0 t}\right) \qquad \text{Eq. 4}$$

N_{seed} is related to $[S]_0$ (Eq. 5), and this leads to Eq.6.

$$N_{seed} = [S]_0 N_A V \qquad \text{Eq. 5}$$

$$L_{grown}(t) = \frac{1}{N_{agg/L}} \frac{[U]_0}{[S]_0} \left(1 - e^{-2k[S]_0 t}\right) \qquad \text{Eq. 6}$$

The experimentally determined length, *L*(*t*), however, also includes that of the seed, L_{seed}, and this needs to be taken into account in the final model (Eq. 7).

$$L(t) = \frac{1}{N_{agg/L}} \frac{[U]_0}{[S]_0} \left(1 - e^{-2k[S]_0 t}\right) + L_{seed} \qquad \text{Eq. 7}$$

We investigated the effect of initial unimer concentration on the growth of PFS_{63}-*b*-$PDMS_{513}$ fiber-like micelles. Varying the initial unimer concentration (from 10 to 30 mg/mL) while keeping the concentration of common solvent and seed concentration constant, resulted in different unimer-to-seed ratios and therefore different final micelle lengths. These (L_n = 613 ± 106, 982 ± 139 and 1798 ± 180 nm for $[U]_0$ = of 10, 20 and 30 mg/mL, respectively) were the same to the 3σ confidence level as the theoretically predicted lengths (L_n = 516, 973, 1431 nm for $[U]_0$ = 10, 20 and 30 mg/mL, respectively), and thus demonstrated the appropriateness of Eq. 7 in this regard. Despite having different final lengths we expected all micelles to have the same linear aggregation number based on the SAXS/WAXS data for the short and long cylindrical micelles discussed above. The time required for the micelles to reach their final length, however, was approximately the same for all 3 experiments (Figure 1 and 2a).

If Eq. 7 correctly describes the micellar length as a function of time, then a plot of the logarithm of L_∞ - $L(t)$, which approximates to L_{final} - $L(t)$, *versus t* should generate a straight line. This, however, was not found to be the case (r-squared = 0.61-0.82) and neither did the data afford a straight-line plot for $1/(L_{final} - L(t))$ *versus t* (r-squared = 0.86-0.94), which would be characteristic of a second order reaction (Figure 1). Non-integer reaction orders can be evaluated by the initial rates method, which involves analysis of the linear region of the L_{final} - $L(t)$ *vs. t* plot (Figure S2). A log-log plot of these rates *vs.* $[U]_0$ then yields the reaction order as the gradient of the line (Figure S3). This method gave an order of 1.16 ± 0.25 with respect to the concentration of unimer, which contrary to the $\ln(L_{final} - L(t))$ *vs. t* plot suggests that the reaction is first-order. This discrepancy, however, is most likely a result of the reduced data set used in the initial rates method, which does not capture the larger deviation from first-order behaviour that occurs at later time points. We therefore explored other data fitting approaches to extract rate information from our experimental data.

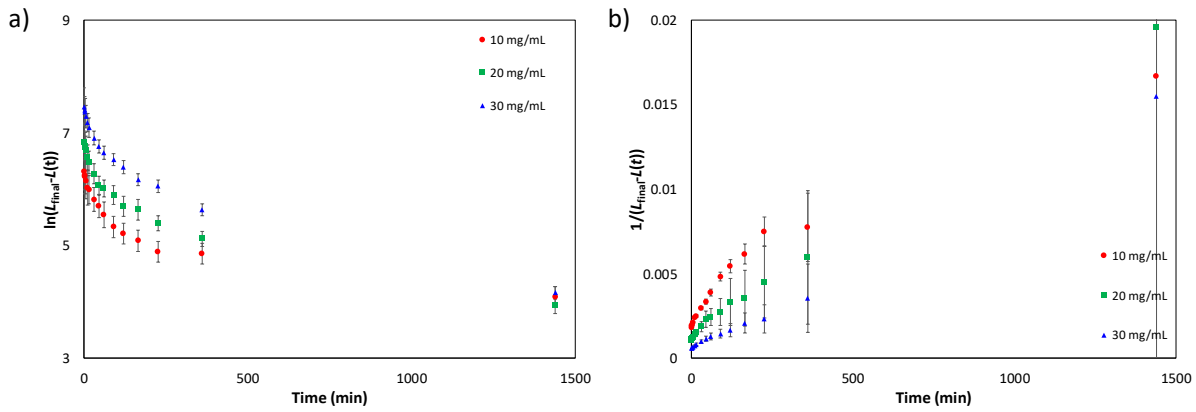

Figure 1: Lengths of PFS_{63}-*b*-$PDMS_{513}$ micelles as a function of time, monitored over a period of 24 h after the addition of unimer (16 μL of 10, 20 or 30 mg/mL of PFS_{63}-*b*-$PDMS_{513}$ THF solution, respectively) to 200 μL of a 0.1 mg/mL PFS_{63}-*b*-$PDMS_{513}$ seed micelles in EtOAc, (L_n = 57 nm, L_w/L_n = 1.11), a) first order plot of $\ln(L_{final} - L(t))$ *versus* time for different unimer concentrations b) second order plot of $1/(L_{final} - L(t))$ *versus* time for different unimer concentrations. Error bars propagated from ±σ (standard deviation) of the micelle length distribution.

Effect of seed concentration

We investigated the effect of seed concentration (1.0×10^{-2}, 6.7×10^{-3} and 3.3×10^{-3} mg/mL) while keeping the initial concentration of unimer and common solvent constant. This resulted in different unimer-to-seed ratios and therefore different final micelle lengths (L_n = 613 ± 106, 919 ± 101 and 1664 ± 13 nm for $[S]_0 = 1.0 \times 10^{-2}$, 6.7×10^{-3} and 3.3×10^{-3} mg/mL, respectively), in a similar manner to varying the initial unimer concentration. As before, these values were within 3σ of the theoretically predicted lengths (L_n = 516, 746 and 1429 nm for $[S]_0 = 1.0 \times 10^{-2}$, 6.7×10^{-3} and 3.3×10^{-3} mg/mL, respectively). The time required for the micelles to reach their final length, however, was slightly different for the 3 concentrations, and the precise form of this data will be discussed in detail in the Data Fitting Section.

Eq. 1 indicates that the rate of unimer consumption should be first order in [*S*], if the reaction kinetics are analogous to those of a living covalent polymerisation. With regards to the rate of micelle growth, however, the situation is slightly different. Differentiating Eq. 7 and examining the initial rate ($2k[S]_0t \ll 1$) demonstrates that $dL/dt \simeq 2[U]_0k/N_{agg/L}$, which is independent of $[S]_0$. The condition of

constant $[U]_0$ required to probe the effect of varying $[S]_0$, however, is also only true at low extents of growth. We therefore determined initial rates at each seed concentration (Figure S4), and represented the data as a function of $[S]_0$ in the form of a log-log plot (Figures S5). This afforded a reaction order of -0.75 ± 0.05 in the concentration of seeds, which is not consistent with the expected zero-order kinetics of micelle growth. The method of initial rates can have limitations in that reaction complexities may not be reflected over the short time-frame that the initial rate can be extracted. We therefore sought a model that could fit the data over the whole course of the reaction.

Data Fitting

To model the change in micelle length with time we attempted to fit the data with single, double, triple, and stretched exponential functions (see Supporting Information, page 12 for more details). A single exponential resulted in underestimation of the final micelle length, as expected from the non-linear nature of the $\ln(L_{final} - L(t))$ *vs.* t plot (Figure 1a). Furthermore, a triple exponential resulted in data over-fitting and therefore large uncertainties associated with the fitted parameters. Both the double and stretched exponential functions enabled us to fit the data well, producing reduced r-squared values of greater than 0.95. To determine which equation consistently gave the better fit, we compared the two models using Akaike's and the Bayesian information criterion tests. In over 80% of cases the stretched exponential was found to provide a better fit of the data (r-squared values > 0.98 all cases), and for the situations where the double exponential was favoured, the difference in reduced r-squared values for the two models was found to be less than 0.5% (Table S2). As the former involved fewer fitted parameters, we concluded that it gave a satisfactory description of the underlying chemical reaction, and that the introduction of further parameters was not justified. The stretched exponential takes the form shown in Eq. 8, where $L(t)$ is the micelle length as a function of time, A is final micelle length minus seed length, k' is the rate constant, b is the fractional power of the exponential, which describes the deviation from a true single exponential and L_{seed} is the seed length (a constant). The contour length for each batch of seeds prepared was measured prior to the kinetics experiments and therefore L_{seed} is fixed as this predetermined value in Eq. 8 (See Supporting Information page 7 for more details).

$$L(t) = A\left(1 - e^{-(k't)^b}\right) + L_{seed} \qquad \text{Eq. 8}$$

Employing Eq. 8 to model the change in length as of function time for different unimer concentrations (Figure 2a, c) affords *k'* values of 1.81 ± 0.19×10^{-4}, 2.13 ± 0.23×10^{-4} and 1.91 ± 0.15×10^{-4} s^{-1} for $[U]_0$ values of 10, 20 and 30 mg/mL, respectively. These rate constants are the same within experimental error. It is noteworthy that the *b* values, which are 0.57, 0.60 and 0.58 for 10, 20 and 30 mg/mL, respectively, are also the same to within experimental error.

For the initial seed concentration data (Figure 2b, d), a fit of Eq. 8 produces *k'* values of 1.81 ± 0.19×10^{-4}, 1.80 ± 0.26×10^{-4} and 1.26 ± 0.14×10^{-4} s^{-1} for $[S]_0$ values of 1.0×10^{-2}, 6.7×10^{-3} and 3.3×10^{-3} mg/mL. Although the rate constants at the highest 2 concentrations are almost identical when the experimental errors are considered, that at the lowest concentration is significantly lower. Comparison of Eqs. 7 and 8, however, show that $k' = 2k[S]_0$, and therefore, unlike the case with $[U]_0$, *k*' is not independent of $[S]_0$. Nonetheless, when *k'* is converted to the $[S]_0$ independent rate constant, *k*, values of 0.009 ± 0.001, 0.013 ± 0.002 and 0.019 ± 0.002 mL/mg.s are obtained for initial concentrations of 1.0×10^{-2}, 6.7×10^{-3} and 3.3×10^{-3} mg/mL, respectively. The reasons for this behaviour are currently unclear, although the inverse relationship between *k* and $[S]_0$ is not what would be expected if the process were diffusion limited, nor if there were systematic error in $[S]_0$. The fits also afford values of 0.57 ± 0.02, 0.62 ± 0.03 and 0.62 ± 0.02 for *b*, of which the former 2 are the same within experimental error with *b* at the lowest concentration marginally larger than that at the highest.

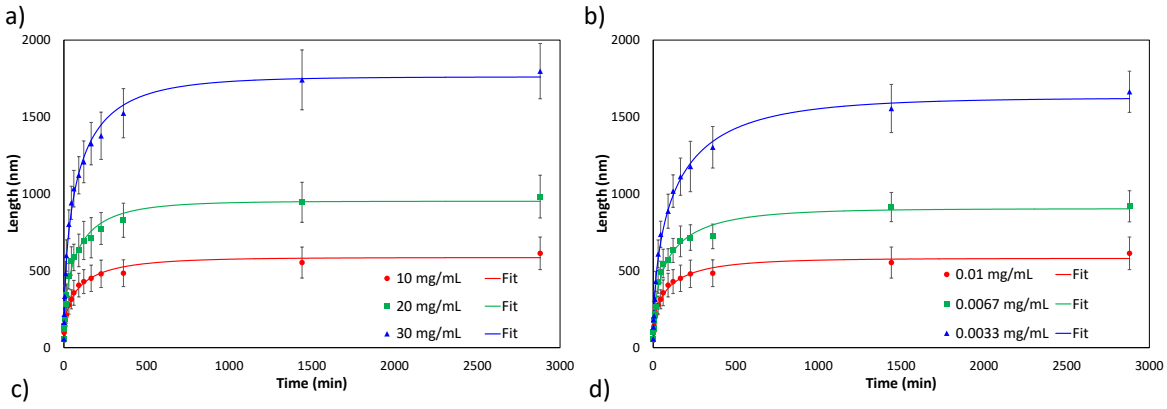

Unimer concentration	A (nm)	Error (nm)	k' (s^{-1})	Error (s^{-1})	b	Error
10 mg/mL	528	13	1.81×10^{-4}	1.9×10^{-5}	0.57	0.02
20 mg/mL	888	23	2.13×10^{-4}	2.3×10^{-5}	0.60	0.02
30 mg/mL	1696	34	1.91×10^{-4}	1.5×10^{-5}	0.58	0.02

Seed concentration	A (nm)	Error (nm)	k' (s^{-1})	Error (s^{-1})	b	Error
1.0×10^{-2} mg/mL	528	13	1.81×10^{-4}	1.9×10^{-5}	0.57	0.02
6.7×10^{-3} mg/mL	826	61	1.80×10^{-4}	2.6×10^{-5}	0.62	0.03
3.3×10^{-3} mg/mL	1553	49	1.26×10^{-4}	1.4×10^{-5}	0.62	0.02

Figure 2: Lengths of PFS_{63}-*b*-$PDMS_{513}$ micelles as a function of time, monitored over a period of 2 days after the addition of unimer to PFS_{63}-*b*-$PDMS_{513}$ seed micelles, (L_n = 57 nm, L_w/L_n = 1.11) for a) variable unimer concentration (16 μL of 10, 20 or 30 mg/mL PFS_{63}-*b*-$PDMS_{513}$ THF solution, respectively and 200 μL of 0.1 mg/mL PFS_{63}-*b*-$PDMS_{513}$ seed micelles in EtOAc), and b) variable seed concentration. (16 μL of 10 mg/mL PFS_{63}-*b*-$PDMS_{513}$ THF solution, and 67, 134 and 201 μL of 0.1 mg/mL PFS_{63}-*b*-$PDMS_{513}$ seed micelles in EtOAc, respectively), c, d) Table of kinetic data for a) variable unimer concentration, b) variable seed concentration, respectively, *A* (nm) = final micelle length minus seed side. a, b) Error bars = ±σ (standard deviation) of the micelle length distribution. c, d) Standard errors for the values *A*, *k'*, and *b* obtained from the fit of Eq.8 to data.

Effect of temperature

To explore the effect of temperature on the growth process, living CDSA experiments involving the addition of PFS_{63}-*b*-$PDMS_{513}$ to crystallite seeds of the same BCP (L_n = 57 nm) were performed at 7 different temperatures; 5, 10, 15, 21, 28, 35 and 42 °C. Elevating the self-assembly temperature increased the length of time required for the micelles to reach their final lengths (Figure 3a and S6) with concomitant reductions in *k'* from 9.09×10^{-4} to 1.21×10^{-5} s^{-1} (Figure 3b). There was also a general trend for a reduction in the *b* values (0.68 to 0.47) and final micelle length achieved with increasing temperature. Specifically, the final micelle length decreased from 3314 ± 279 nm to 1764 ± 209 nm, as the temperature was increased from 5 to 42 °C. The most likely cause of this change would be an increase in micellar width and, consequently, in $N_{agg/L}$ with temperature. This is similar to the reported thickening in the chain axis direction of homo- and random copolymer crystals on thermal annealing.[93,94] Indeed, SAXS on the final micelle solutions revealed an increase in core cross-sectional area from 41 to 76 nm^2 on increasing the temperature from 5 to 42 °C (Figure S7 and Table S3). It would be expected for this to scale with the decrease in *L*, if change in cross-sectional area were the sole contributor. This was not the case, however, with the 47% decrease in length being associated with an 85% increase in cross-sectional area. Furthermore, WAXS indicated that the inter-chain spacing within the cores of the two different micellar samples was the same (Figure S7c). A possible explanation for this discrepancy could be the transition from a rectangular to a more elliptical

cross-section for the micelle on increasing the growth temperature. From the rate constants for the experiments at different temperatures we were able to generate an Eyring plot to determine the mean activation enthalpy, entropy and free energy for the reaction (from the data presented in Figure 3a). This provided negative values for the enthalpic and entropic activation terms (Figure S8) of -89.0 kJ/mol and -619 J/mol, respectively.

a)

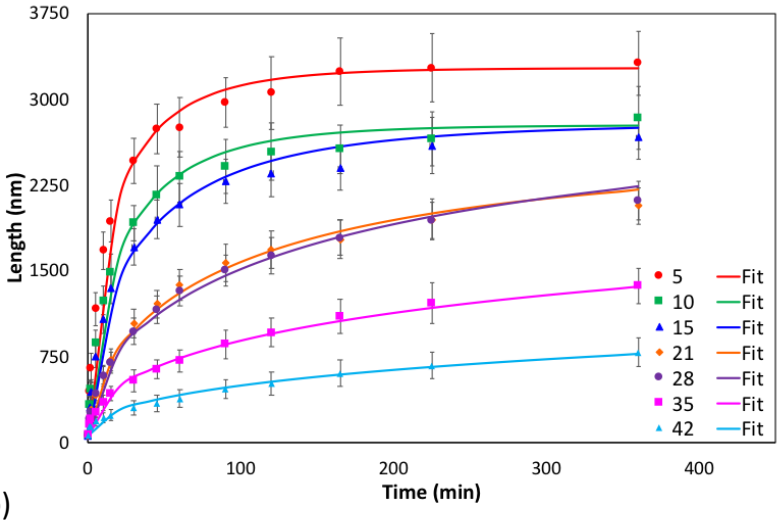

b)

Temp (°C)	A (nm)	Error (nm)	k' (s^{-1})	Error (s^{-1})	b	Error
5	3177	44	9.09×10^{-4}	5.4×10^{-5}	0.68	0.02
10	2630	42	7.51×10^{-4}	4.8×10^{-5}	0.70	0.02
15	2630	51	5.18×10^{-4}	4.2×10^{-5}	0.64	0.02
21	2404	52	1.67×10^{-4}	1.4×10^{-5}	0.60	0.02
28	2817	42	9.38×10^{-5}	6.1×10^{-6}	0.55	0.01
35	2161	32	3.85×10^{-5}	2.9×10^{-6}	0.50	0.01
42	1698	60	1.21×10^{-5}	2.1×10^{-6}	0.47	0.01

Figure 3: a) Lengths of PFS_{63}-*b*-$PDMS_{513}$ micelles as a function of time, monitored over a period of 6 h after the addition of unimer to PFS_{63}-*b*-$PDMS_{513}$ seed micelles (L_n = 57 nm, L_w/L_n = 1.11) (24 μL of 20 mg/mL PFS_{63}-*b*-$PDMS_{513}$ THF solution, and 200 μL of 0.1 mg/mL PFS_{63}-*b*-$PDMS_{513}$ seed micelles in EtOAc). b) Table of kinetic data for variable temperature studies. a) Error bars = ±σ (standard deviation) of the micelle length distribution. b) Standard errors for the values *A*, *k'*, and *b* obtained from the fit of Eq.8 to data.

Effect of solvent

To investigate the effect of common solvent on the growth kinetics, 3 different THF compositions were examined, namely 2.3, 4.8 and 9.7% v/v THF in *n*-hexane. As the THF content increased, the growth rate of the micelles slowed as evidenced by k' = 1.56×10^{-2}, 3.04×10^{-3} and 4.57×10^{-4} s^{-1} for 2.3, 4.8 and 9.7% v/v THF, respectively (Figure 4a, c and S9 and S10). This reduction in rate constant, however, is accompanied by an increase in *b*, which is the opposite of the trend observed for the experiments performed at different temperatures. It is noteworthy, however, that although all experiments showed convergence to a constant final *L*, this is around the 3σ confidence limit above the length predicted from the seed size and unimer to seed ratio (628 nm).

In order to probe the role of the selective solvent on the rate of the self-assembly process, solvents with differing solubility parameters were chosen: *n*-hexane (14.9 $MPa^{1/2}$), *n*-heptane (15.3 $MPa^{1/2}$), and ethyl acetate (18.2 $MPa^{1/2}$).[95] Other solvents were also explored, but it proved difficult to analyze the resulting micelles by TEM, due to severe aggregation or fragmentation upon drying (see Supporting Information, page 19 for more details). The rate constants decreased on exchanging *n*-hexane for *n*-heptane and then ethyl acetate (k' = 6.32×10^{-3}, 3.45×10^{-3} and 1.75×10^{-5} s^{-1}, respectively), whilst maintaining a constant THF composition of 4.8% v/v. These experiments demonstrated that as the medium becomes a less poor solvent for the insoluble core-forming PFS block (18.7 $MPa^{1/2}$, PDMS = 14.9 $MPa^{1/2}$),[96] the rate constant decreases (Figure 4b, d and S11). Although the series: *n*-hexane, *n*-heptane, and ethyl acetate became concomitantly poorer for the PDMS corona-forming block, there was no evidence of reverse micelle formation or any decrease in the colloidal stability of the resulting micelles. This suggests that the effect of the solvent on the crystallization of the core is more significant in determining the rate constant than the change in amphiphilicity of the copolymer. A trend of increasing *b* as the solvent medium became better for PFS was also observed, similar to that for the experiments with different concentrations of common solvent (THF). Once again, the similar final micelle lengths (L_n = 837 ± 79, 876 ± 89 and 956 ± 116 nm for *n*-hexane, *n*-heptane and EtOAc, respectively) were comparable and within 3σ of the predicted length (628 nm), which suggested that there was no significant change in linear aggregation number on changing the selective solvent. It is noteworthy that the micelles grown in ethyl acetate were slightly shorter than those

grown in *n*-heptane and *n*-hexane after 24 h (1440 min, Figure 4b), but after 1 month the final micelle lengths were the same within error (Figure S11).

a)

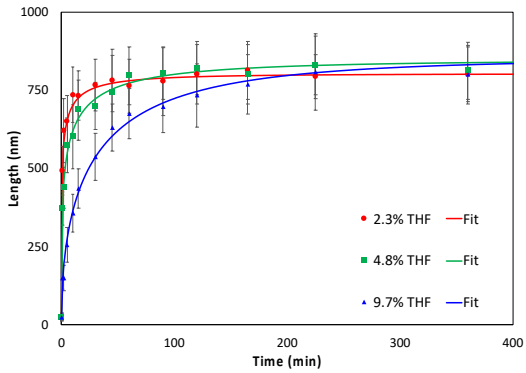

b)

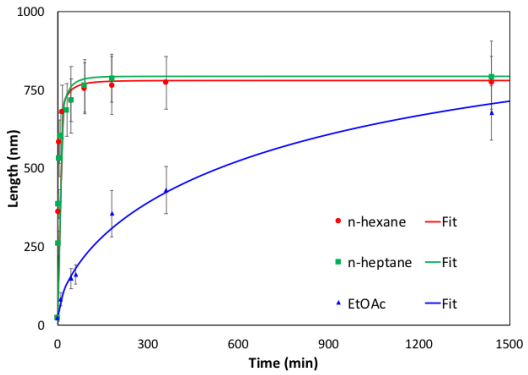

c)

THF (%)	A (nm)	Error (nm)	k' (s^{-1})	Error (s^{-1})	b	Error
2.3	790	12	1.56×10^{-2}	3.3×10^{-3}	0.31	0.04
4.8	832	14	3.04×10^{-3}	3.9×10^{-4}	0.35	0.02
9.7	855	24	4.57×10^{-4}	5.9×10^{-4}	0.55	0.03

d)

Solvent	A (nm)	Error (nm)	k' (s^{-1})	Error (s^{-1})	b	Error
n-hexane	734	8	6.32×10^{-3}	5.0×10^{-4}	0.49	0.03
n-heptane	748	16	3.45×10^{-3}	3.4×10^{-4}	0.54	0.06
EtOAc	928	32	1.75×10^{-5}	2.7×10^{-6}	0.62	0.03

Figure 4: Lengths of PFS_{63}-*b*-$PDMS_{513}$ micelles as a function of time, monitored over a period of a) 6 h and b) 24 h after the addition of unimer to PFS_{63}-*b*-$PDMS_{513}$ seed micelles, (L_n = 25 nm, L_w/L_n = 1.25) for a) variable percentage THF (48 μL of 10 mg/mL PFS_{63}-*b*-$PDMS_{513}$ THF solution, and 200μL of 0.1 mg/mL PFS_{63}-*b*-$PDMS_{513}$ seed micelles in *n*-hexane), and b) variable selective solvent (48 μL of 10 mg/mL PFS_{63}-*b*-$PDMS_{513}$ THF solution, and 200μL of 0.1 mg/mL PFS_{63}-*b*-$PDMS_{513}$ seed micelles in *n*-hexane). c), d) Table of kinetic data for a) variable percentage THF, b) variable selective solvent, respectively. a, b) Error bars = ±σ (standard deviation) of the micelle length distribution. c, d) Standard errors for the values *A*, *k'*, and *b* obtained from the fit of Eq.8 to data.

Effect of PFS degree of polymerization

To investigate the effect the degree of polymerization of the PFS core has on the micelle growth rate, kinetic experiments were also performed with the BCPs, PFS_{63}-*b*-$PDMS_{513}$ and PFS_{49}-*b*-$PDMS_{504}$ (block ratios 1:8 and 1:10, respectively). These BCPs were selected as they have very similar degrees of polymerization for the corona-forming block (difference < 2 %), but PFS_{49}-*b*-$PDMS_{504}$ has a core-forming PFS block which has a degree of polymerization 22% lower than for PFS_{63}-*b*-$PDMS_{513}$. Reducing the PFS degree of polymerization not only reduced the micelle growth rate (from *k'* = 1.16

± 0.08×10^{-4} s^{-1} to *k'* = 4.6 ± 0.7×10^{-6} s^{-1}), but also resulted in much shorter micelles being formed (L_n = 2690 ± 253 nm and 1426 ± 134 nm for PFS_{63}-*b*-$PDMS_{513}$ and PFS_{49}-*b*-$PDMS_{504}$, respectively) (Figure 5). We viewed this as a likely consequence of the linear aggregation number being different for the two types of micelle on account of the different BCPs employed. To investigate this hypothesis further, solution SAXS/WAXS was performed on the final micelles grown from PFS_{63}-*b*-$PDMS_{513}$ and PFS_{49}-*b*-$PDMS_{504}$. These revealed a likely increase in core cross-sectional area from 70 ± 6 to 78 ± 9 nm^2 on reducing the PFS length from DP_n = 63 to 49 (Figure S12 and Table S4) with no significant change in the associated core structure. The linear aggregation numbers are therefore 3.7 ± 0.3 and 5.4 ± 0.6 chains/nm for PFS_{63}-*b*-$PDMS_{513}$ and PFS_{49}-*b*-$PDMS_{504}$, respectively, and this increase of 46% almost fully accounts for the observed 47% reduction in final micelle length. More strikingly, the kinetic data demonstrate that reducing the PFS core length by an average of 14 repeat units caused the rate constant to be reduced by a factor of 25 from a *k'* value of 1.16 ± 0.08×10^{-4} s^{-1} for PFS_{63}-*b*-$PDMS_{513}$ to 4.6 ± 0.7×10^{-6} s^{-1} for PFS_{49}-*b*-$PDMS_{504}$. It is also noteworthy that different *b* values were obtained from the fits (*b* = 0.60 ± 0.01 and 0.53 ± 0.02 for PFS_{63}-*b*-$PDMS_{513}$ and PFS_{49}-*b*-$PDMS_{504}$, respectively).

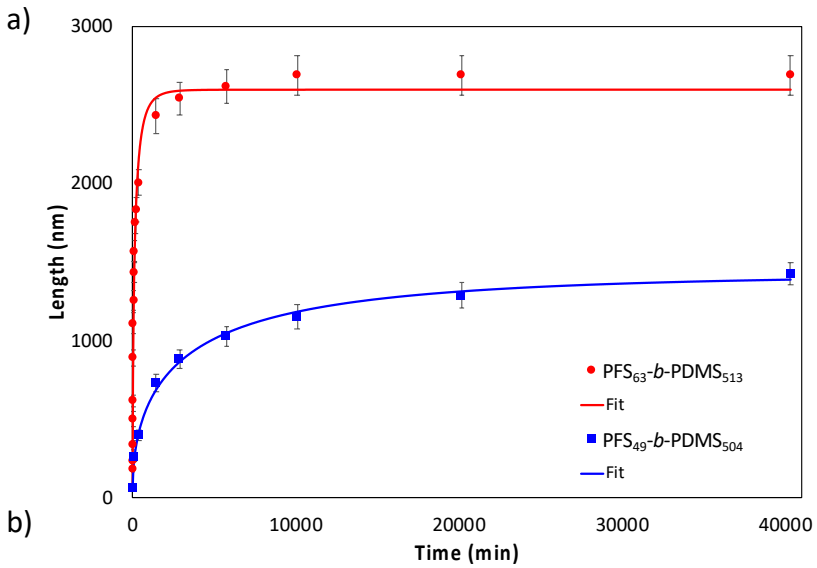

PFS Length	A (nm)	Error (nm)	k' (s^{-1})	Error (s^{-1})	b	Error
PFS_{63}-*b*-$PDMS_{513}$	2520	42	1.16×10^{-4}	7.8×10^{-6}	0.60	0.01
PFS_{49}-*b*-$PDMS_{504}$	1376	45	4.59×10^{-6}	6.7×10^{-7}	0.53	0.02

Figure 5: a) Lengths of PFS-*b*-PDMS micelles as a function of time, monitored over a period of 4 weeks after the addition of unimer to PFS_{63}-*b*-$PDMS_{513}$ seed micelles (L_n = 57 nm, L_w/L_n = 1.11), (48 μL of 10 mg/mL PFS_{63}-*b*-$PDMS_{513}$ THF solution, or 48 μL of 9.25 mg/mL PFS_{49}-*b*-$PDMS_{504}$ THF solution, and 200μL of 0.1 mg/mL PFS_{63}-*b*-$PDMS_{513}$ seed micelles in EtOAc). b) Table of kinetic data for changing PFS core length. a) Error bars = ±σ (standard deviation) of the micelle length distribution. b) Standard errors for the values *A*, *k'*, and *b* obtained from the fit of Eq.8 to data.

Monitoring micelle growth using super-resolution fluorescence microscopy

It is important to verify that the data we have obtained from the TEM analysis of dried samples characterizing the growth of PFS_{63}-*b*-$PDMS_{513}$ cylindrical micelles is representative of the CDSA process that occurs in solution. It has already been established for fully assembled micelles that the super-resolution techniques STED and SMLM provide comparable results to TEM.[87] However, for the kinetics experiments all techniques were performed with high concentrations of unassembled unimer at early time points, which could, in principle, add to the micelle termini during the drying process. We therefore followed the micelle growth using SRFM as a solution-based technique to validate the trends obtained from TEM experiments. We have recently established protocols for use in organic media with the BCP PFS_{56}-*b*-$PDMS_{775}$/DYE_{20}.[87] For both techniques, short fluorescent seed micelles were prepared from BCPs 3% labelled with the appropriate dye, STAR635 (STED) and CAGE635 (SMLM). The fluorescent seed micelles were longer (L_n = ca. 600 nm) than those typically used (L_n = 25-57 nm) to aid visualization of the structures during the experiments, particularly at the early time points where the unimer concentration remains relatively high, which limits the signal to background ratio. Fluorescently labelled BCP unimer (dye = STAR635 single colour STED, CAGE500 for dual-colour SMLM) was added to the short fluorescent seed micelles and aliquots were taken from the solution and analyzed by STED, SMLM and TEM (Figure 6 and S13).

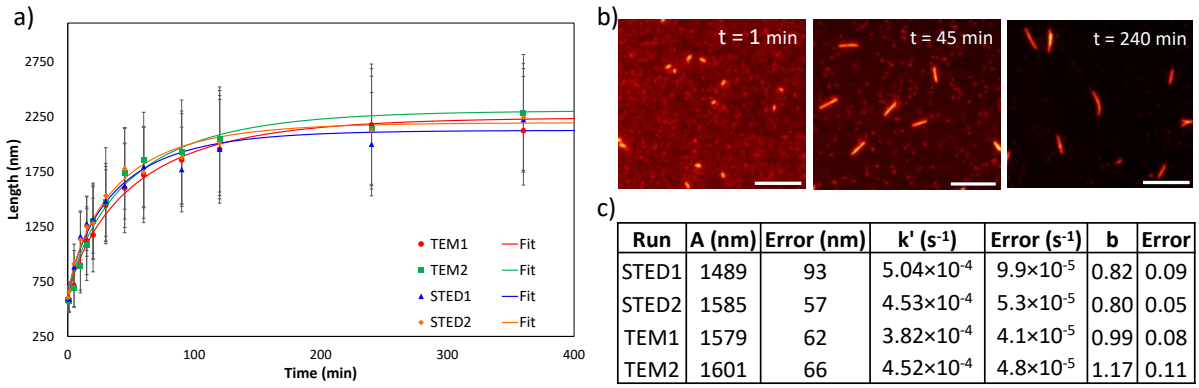

c)

Run	A (nm)	Error (nm)	k' (s^{-1})	Error (s^{-1})	b	Error
STED1	1489	93	5.04×10^{-4}	9.9×10^{-5}	0.82	0.09
STED2	1585	57	4.53×10^{-4}	5.3×10^{-5}	0.80	0.05
TEM1	1579	62	3.82×10^{-4}	4.1×10^{-5}	0.99	0.08
TEM2	1601	66	4.52×10^{-4}	4.8×10^{-5}	1.17	0.11

Figure 6: a) Plot of micelle length against time for TEM run 1 and 2 and STED run 1 and 2, monitored over a period of 6 h, 6.5 µL of 10 mg/mL PFS_{56}-*b*-$PDMS_{775}$/$STAR635_{20}$ THF solution and 200 µL of 0.15 mg/mL short STAR635-fluorescent micelles (L_n = 577 nm, L_w/L_n = 1.03) in EtOAc. b) representative STED images at time points 1 min, 45 min and 240 min. Scale bars = 4.8 µm. c) Table of kinetic data for STAR635 BCP analyzed by STED and TEM. a) Error bars = ±σ (standard deviation) of the micelle length distribution. c) Standard errors for the values *A*, *k'*, and *b* obtained from the fit of Eq.8 to data.

For the STED/TEM kinetics experiments, all *k'* values are within error of each other, however, the *b* values obtained from the data fitting for these experiments show quite significant discrepancies between the runs analyzed using STED and those employing TEM. The *b* values from the STED runs are self-consistent (ca. 0.8), but do not agree with the TEM experiments, which provide much larger *b* values (1.0 - 1.1). Furthermore, these contradict the *b* values obtained (0.57 – 0.6) for the self-assembly of the non-dye-labelled BCP (Data Fitting Section). Inspection of the raw TEM data obtained for both the unlabelled and labelled PFS-*b*-PDMS experiments indicate that PFS_{56}-*b*-$PDMS_{775}$/$STAR635_{20}$ produces micelles with higher dispersities (PDI = 1.2-1.3) than PFS_{63}-*b*-$PDMS_{513}$ (PDI = 1.1-1.2). This increase in polydispersity increases the error associated with the length at each time point in the series, and therefore also the uncertainty in the fit. Repeating the fit of the data, but without weighting for the standard deviation of the micelle lengths produced *b* values which were all 0.9 or lower. This indicates the significant role that the errors play in determining the *b*

values obtained, especially given the modest change in dispersity between samples. Nonetheless, even when the error weighting is removed, the STED and TEM *b* values are still not in agreement, and this could be due to the lower resolution of the former effecting the accuracy of the measurement at early time points (*i.e.* shorter lengths). We also studied the micelle growth kinetics using two-colour SMLM (Figure S13 and S14), however, like the STED/TEM results, the techniques were inconsistent with each other, and the TEM data also differed from that obtained with unlabelled BCP. Although consideration of the STED data alone confirmed the non-first order behaviour of CDSA with respect to unimer ($b \neq 1$), as determined by TEM analysis, the necessity for dye-labelled BCP (albeit at only 3%) clearly complicates the self-assembly process. The exact role of the dye is currently unclear, but it evidently increases the rate of addition ($k' = 4.53 \pm 0.53 \times 10^{-4}$ and $1.81 \pm 0.19 \times 10^{-4}$ s^{-1} for with and without dye, respectively), and also the length dispersity of the sample.

Discussion

An investigation of the proposed differential rate equation for living CDSA (Eq. 1), by the method of initial rates, yielded reaction orders for [*U*] and [*S*] of 1.16 ± 0.25 and -0.75 ± 0.05, respectively. Although the estimate of the former was consistent with the first-order behaviour expected by analogy to a living covalent polymerization, the zero-order dependence on [*S*] expected for *L*(t) was not observed. *L*(t), however, exhibited a more complex relationship to both [*U*] and [*S*] when the whole duration of the reaction was considered. The length of PFS_{63}-*b*-$PDMS_{513}$ micelles observed during the self-assembly process as a function of time was therefore best modelled by a stretched exponential function (Eq. 8). In nature, stretched exponential functions have been successfully used to model processes that required a certain protein conformation to be obtained, but which may be achieved from any number of non-functional alternatives. This gives rise to a distribution of activation energies, and thus also to a distribution of kinetic rates, where the parameter *b* (Eq. 8) is related to the width of the distribution. The crystallization of unimer onto the termini of the growing micelle would require the polymer in solution, and at the surface of the micellar core, to adopt a limited number of all the possible conformations, many of which will be energetically similar and accessible at ambient temperature. This situation would give rise to the distribution of activation

energies required for the observed stretched exponential relationship of L with respect to t. It should be noted that there is no requirement for molecular weight polydispersity in this explanation, only that the molecular weight is high enough for energetically similar conformations to be available. Indeed, the supramolecular polymerization of porphyrin-based monomers, where both these complexities are necessarily absent, is first-order with respect to monomer concentration.[49]

It is evident from the experiments performed at different temperatures that increasing the temperature results in a reduced rate constant (k'). This is consistent with reports that the linear growth rate of homopolymer crystals decreased upon lowering the extent of supercooling,[97] and may also be due to increased solubility of the core-forming block on increasing the temperature. However, the different temperature kinetic experiments also revealed that altering the self-assembly temperature effects the dimensions of the final cylindrical micelles in a similar manner to that observed for homopolymer crystals.[98] Cylindrical micelles grown at higher temperatures were shorter in length with larger core radii, and with a higher linear aggregation number (2.2 chains/nm at 5 °C compared to 4.1 chains/nm at 42 °C). It is noteworthy that studies of the annealing of PI_{637}-*b*-PFS_{53} cylindrical micelles in solution revealed no thickening of the micellar core at temperatures below 60 °C.[99] These experiments therefore demonstrate that it is only when growth occurs at elevated temperatures that the micelle structure changes, and that it is temperature rather than the core radius of the seed that determines the radius of the newly grown section. We suggest that the change in $N_{agg/L}$ occurs in the early stages of growth, so as to give a different core cross-sectional area by SAXS, and not a distribution of areas bounded at the low end by that of the seed (scattering from the seed is dominated by that from the newly grown portion on account of the relative amounts). It is noteworthy that no step change in width is seen by TEM, although the ca. 1 nm change is at the resolution limit of the instrument.

The kinetic experiments at different temperatures also allowed us to obtain information regarding the thermodynamics of the activation parameters involved for the living CDSA of PFS_{63}-*b*-$PDMS_{513}$ micelles through an Eyring plot. Both the entropic and enthalpic terms were negative, which is expected due to the increased ordering of the core-forming PFS BCP chains upon crystallization and the exothermic nature of crystallization, respectively.

The solvent composition plays an important role in the rate of micelle growth. Altering the solvent composition so that it is more favourable for the PFS core-forming block, either by increasing the amount of common solvent, or through using a selective solvent that has a solubility parameter closer to that of PFS (*e.g.* using EtOAc instead of *n*-hexane) causes a reduction in the rate constant. This trend underscores how any parameter that reduces the propensity for the PFS segment to precipitate from solution and crystallize on the termini of the growing micelle reduces the micellar growth rate.

It has been reported that altering the overall composition of PFS-containing micelles effects the dimensions of the resulting micellar structure,[89] but no comment was made as to how this might affect the rate of growth. In this experiment, it was found that reducing the number average degree of polymerization of the PFS segment by 22% (14 monomer units) from PFS_{63} to PFS_{49}, whilst keeping the length of the corona block approximately the same (< 2% decrease), resulted in a rate constant (*k*') 25 times smaller. It is known that the solubility of polymer chains decrease as the degree of polymerization increases and, therefore, it is expected that the PFS block will be less soluble in *n*-hexane in the BCP with the longer PFS core-forming segment than that with the shorter block. Furthermore, the equilibrium melting point, T_m, will increase with molecular weight, leading to a larger degree of supercooling for the BCP with the longer PFS block, and this is reported to increase the linear crystal growth rate.[97] Increasing the length of the PFS segment has also been shown to decrease the linear aggregation number, and hence increase the final length of the resulting micelles. An implication of chains of different lengths adding at different rates would be the establishment of a continuum of rates over the molecular weight distribution of the sample, which could give rise to the observed stretched exponential behaviour. We therefore modelled micelle growth, $L(t)$, using an initial Zimm-Schulz distribution of molecular weights, and a scaling factor relating the change in *k'* per unit degree of polymerization (see Supporting Information, page 24 for more details). Using the experimentally determined PDI for the PFS block (1.04) only afforded the typically observed *b* value (*ca*. 0.6) for scaling powers between 4 and 5, and these are far less than the value of 12 observed between the change in DP_n for the core-forming block and corresponding change in *k'*. However, the range of molecular weights constituting the majority of each copolymer sample [$\sigma(M_n)$ = 2373 and

3051 g mol^{-1} for PFS_{49} and PFS_{63}, respectively] is narrower than the separation between PFS_{49}-*b*-$PDMS_{504}$ and PFS_{63}-*b*-$PDMS_{513}$ [ΔM_n(PFS) = 3390 g mol^{-1}]. This may mean that more subtle changes in *k'*(DP_n) exist within a relatively monodisperse copolymer sample, and this is lost on studying two more disparate examples. Nonetheless, this analysis clearly cannot discount a role for core-forming block polydispersity as part of the reason for stretched exponential growth kinetics. It should also be noted that PFS_{63}-*b*-$PDMS_{513}$ with the longer PFS segment added at a faster rate than PFS_{49}-*b*-$PDMS_{504}$, which has a shorter PFS segment, which is the opposite to what would be expected if this were a diffusion limited process.

Previous work has demonstrated how the seed structure at the low length limit (*ca.* 20 nm) differs from that of the resulting micelle, and even the parent micelle from which it is derived.[100] This suggests that it is possibly simplistic to expect totally symmetric growth from either side of the seed, and growth from seeds of all sizes to be the same. The seed size, however, appears to have modest influence on the growth rate with *k'* ($9.8 \pm 1.5 \times 10^{-5}$ s^{-1}) for the longest seed size (915 nm) decreasing below the 3 σ confidence limit of that of the shortest (*k'* = $4.61 \pm 0.65 \times 10^{-4}$ s^{-1} for L_n(seed) = 25 nm). Nonetheless, the similarity of *k'* values ($6.10 \pm 0.42 \times 10^{-4}$ and $3.22 \pm 0.56 \times 10^{-4}$ s^{-1}) when equal amounts of unimer were added to seeds of L_n = 25 and 493 nm, respectively, suggests that the short seeds are not unusual from a kinetics standpoint (see Supporting Information Figures S15-17 and Table S2).

The *in situ* experiments performed using SRFM techniques demonstrated how the stretched exponential also characterizes the observed growth process in solution, validating the data obtained from the TEM experiments. In these experiments, despite only being present on 3% of the corona, the nature of the dye has an effect on the micellar growth rate. The STAR635 dye-labelled BCP has a faster growth rate than the CAGE500-labelled BCP for the SMLM experiments. This effect of dye structure on the growth rate had been ascribed to the required modification of the corona-forming block altering amphiphilicity of the BCP.[101] Finally, for the SRFM experiments the sample preparation methods prevented the addition of any remaining unimer present in the sample to the micelle termini, and therefore effectively quenched the self-assembly reaction. This was convenient as

image acquisition times are typically between 2-10 minutes, depending on the SRFM technique, and it is therefore important that growth is halted prior to analysis.

Conclusion

In summary, we have probed the growth kinetics of living CDSA using PFS -*b*-PDMS BCPs as a model system. We discovered that a range of parameters affect the micellar growth rate including concentration, temperature, the nature of the solvent medium, and BCP composition. It is noteworthy that the rate of self-assembly can be increased by either lowering the temperature, using poorer solvents for the crystalline PFS core-forming block, or by employing BCPs with longer core-forming PFS segments. Data fitting also enabled us to determine that the analogy of living CDSA to a living covalent polymerization of molecular monomers does not apply to the reaction kinetics, and that the growth rate is neither first order in unimer nor in seed concentration. The deviation from first order kinetics could be modelled using a stretched exponential function and we postulate that this behaviour results from a combination of the influences of polymer chain conformation and molecular weight polydispersity on the addition of unimer to the micelle termini. These two factors arise as a natural consequence of the increased complexity of synthetic BCP chains compared to their monodisperse, small molecule counterparts.

Overall, these results provide important additional insight into living CDSA processes and also provide guidelines for optimizing the efficiency of experimental protocols that should be of considerable significance for work with a growing variety of BCPs with crystalline core-forming blocks[32,39,42-44] and analogous amphiphiles[45-56] that can be used for seeded supramolecular polymerizations. In addition, an informative comparison is enabled with analogous biological and synthetic supramolecular systems that undergo fiber formation via nucleation-elongation processes. For example, the low length polydispersities and kinetic data obtained for living CDSA underscore the virtual absence of heterogeneous growth rates where some 1D nanoparticles grow substantially faster than others, which has been observed for the case of certain protein fibers and has been attributed to fiber polymorphism.[44]

Methods

General Experimental Considerations

Anionic polymerizations were carried out in an argon atmosphere glovebox. All other manipulations were carried out under an open atmosphere unless otherwise stated. All block copolymers were prepared by the sequential living anionic polymerization of dimethylsila[1]ferrocenophane and hexamethylcyclotrisiloxane, as previously reported.[87,88] All reagents were purchased from Sigma-Aldrich unless otherwise stated. Monomer purifications were performed under an atmosphere of purified N_2. THF was distilled from Na/benzophenone immediately before use. The dyes STAR635 NHS ester and CAGE635 NHS ester were purchased from Abberior GmbH. Photoirradiation experiments were carried out with Pyrex-glass filtered emission from a 125 W medium-pressure mercury lamp (Photochemical Reactors Ltd.). An ethylene glycol/water bath in conjunction with a thermostat was used to maintain constant temperatures of 20 °C during the photoirradiation experiments. ^{1}H and ^{13}C NMR spectra were recorded using Jeol Eclipse 400 MHz or Varian VNMR 400 MHz spectrometers.

Polymer Characterization

Gel permeation chromatography was carried out using a Viscotek VE 2001 Triple-Detector Gel Permeation Chromatograph equipped with an automatic sampler, a pump, an injector, an inline degasser, and a column oven (30 °C). The elution columns consist of styrene/divinylbenzene gels with pore sizes between 500 Å and 100,000 Å. Detection was conducted by means of a VE 3580 refractometer, a four-capillary differential viscometer, and 90° and low angle (7°) laser light (λ_0= 670 nm) scattering detectors, VE 3210 & VE 270. THF (Fisher) was used as the eluent, with a flow rate of 1.0 mL/min. Samples were dissolved in the eluent (2 mg/mL) and filtered with a Ministart SRP 15 filter (polytetrafluoroethylene membrane of 0.45 μm pore size) before analysis. The calibration was conducted using a PolyCAL™ polystyrene standard (PS115K) from Viscotek. Matrix-assisted laser desorption/ionization time of flight (MALDI-TOF) mass spectrometry measurements of polyferrocenyldimethylsilane (PFDMS) were performed using a Bruker Ultraflextreme running in linear mode. Samples were prepared using a trans-2-[3-(4-*tert*-butylphenyl)-2-methyl-2-propenylidene]malononitrile matrix (20 mg/mL in THF) and the polymer sample (2 mg/mL in THF),

mixed in a 10:1 (v/v) ratio. Approximately 1 µL of the mixed solution was deposited onto a MALDI sample plate and allowed to dry in air. The molecular weights of the diblock copolymers were then determined by combining the molecular weight M_n of the first block from MALDI-TOF measurements with the block ratio of the diblock copolymer obtained by integrating the ^{1}H NMR spectroscopic signal intensities of the respective blocks.

Transmission electron microscopy (TEM)

Copper grids from Agar Scientific, mesh 400, were coated with a carbon film. Carbon coating was done using an Agar TEM Turbo Carbon Coater where carbon was sputtered onto mica sheets before deposition on the copper grids *via* flotation on water. Bright field TEM micrographs were obtained on a JEOL1200EX II microscope operating at 120 kV and equipped with an SIS MegaViewIII digital camera.

Stimulated emission depletion (STED) microscopy

STED imaging was performed on a home-built pulsed STED microscope described in detail in the following reference.[102] Briefly, the excitation and STED beam are obtained from a single titanium-sapphire oscillator centered at λ_{STED} = 765 nm (Ti:S, Mai Tai HP, Spectraphysics). The excitation beam, centered at λ_{ex} = 640 nm, was extracted from a supercontinuum source (FemtoWhite, NKT Photonics) by a bandpass filter (637/7 BrightLine HC, Semrock) and coupled into a polarization maintaining single-mode fiber (PM630-HP, Thorlabs). The pulse duration of the STED beam was stretched to approximately 100-200 ps thanks to a 50 cm glass block of SF66 (IC Optical Systems, United Kingdom) and 100 m long polarization maintaining single-mode fiber (PM-S630-HP, Thorlabs). Additionally the STED beam was shaped into a donut beam by a spatial light modulator (X10468−02, Hamamatsu). The excitation and STED beam were recombined with a dichroic mirror (T735spxr, Chroma) and sent to a commercial point-scanning microscope (Abberior Instruments) comprising: a microscope frame (IX83, Olympus), a set of galvanometer mirrors (Quad scanner, Abberior Instruments) and a detection unit. The beams were focused onto the sample by a 100×/1.4 NA oil immersion objective lens (UPLSAPO 100XO, Olympus) and images were acquired by raster scanning the beams across the sample using the Inspector Image Acquisition software (Andreas

Schönle, Abberior Instruments GmbH, Göttingen, Germany). Typically a field of view of 80×80 μm^2 was used with a pixel size of 20×20 nm^2 and pixel dwell times of 30 µs and 50 µs respectively. Moreover, each line was scanned successively five times with a pixel dwell time of 10 µs per line-scanning. Fluorescence photons emerging from the sample were collected by the microscope objective lens, de-scanned by the galvanometer mirrors, focused onto a pinhole and sent to an avalanche photodiode (SPCM-AQRH, Excelitas Technologies). Laser powers, measured at the objective back aperture, were ~20-30 µW for the excitation beam and ~100-150 mW for the STED beam.

Acknowledgements

C.E.B. thanks the Bristol Chemical Synthesis Centre for Doctoral Training, funded by the EPSRC for the provision of a PhD studentship. E. M. L acknowledges the EU for a Marie Curie postdoctoral fellowship. D.W.H. was supported by the EPSRC Bristol Cente for Functional Nanomaterials doctoral training grant [EP/G036780/1]. R. F. L., P. M. and C.F.K. acknowledge grants from the EPSRC, UK (grant EP/H018301/1, EP/L015889/1) and the Medical Research Council (grant MR/K015850/1). I.M. thanks the EU for an ERC Advanced Investigator Grant. TEM studies were carried out in the Chemistry Imaging Facility at UoB with equipment funded by UoB and EPSRC (EP/K035746/1). The authors would like to thank David J. Lunn, John R. Finnegan, and Jieshu Qian for helpful discussions and Dr. Torben Gädt for preliminary experiments on the micelle growth kinetics.

Author Contributions

C. E. B. and E. M. L. performed all experiments, data analysis and wrote the paper together with R. F. L., G. R. W., C. F. K. and I. M. and additional scientific input was provided by D.W.H., G. G., and M. A. W. D. W. H. performed the X-ray analysis and assisted with the data fitting along with R. F. L., P. M. and R. M. R. The STED and SMLM was performed by P. M. and R. F. L., respectively. C. F. K. and I. M. supervised the project.

References

(1) De Greef, T. F. A.; Smulders, M. M. J.; Wolffs, M.; Schenning, A. P. H. J.; Sijbesma, R. P.; Meijer, E. W. Supramolecular Polymerization. *Chem. Rev.* **2009**, *109*, 5687–5754.

(2) Whitesides, G. M. Self-Assembly at All Scales. *Science* **2002**, *295*, 2418–2421.

(3) Schacher, F. H.; Rupar, P. A.; Manners, I. Functional Block Copolymers: Nanostructured Materials with Emerging Applications. *Angew. Chem. Int. Ed.* **2012**, *51*, 7898–7921.

(4) Mai, Y.; Eisenberg, A. Self-Assembly of Block Copolymers. *Chem. Soc. Rev.* **2012**, *41*, 5969–5985.

(5) Wang, J.; Liu, K.; Xing, R.; Yan, X. Peptide Self-Assembly: Thermodynamics and Kinetics. *Chem. Soc. Rev.* **2016**, *45*, 5589–5604.

(6) Hayward, R. C.; Pochan, D. J. Tailored Assemblies of Block Copolymers in Solution: It Is All about the Process. *Macromolecules* **2010**, *43*, 3577–3584.

(7) Gröschel, A. H.; Walther, A.; Löbling, T. I.; Schacher, F. H.; Schmalz, H.; Müller, A. H. E. Guided Hierarchical Co-Assembly of Soft Patchy Nanoparticles. *Nature* **2013**, *503*, 247-251.

(8) Blanazs, A.; Armes, S. P.; Ryan, A. J. Self-Assembled Block Copolymer Aggregates: From Micelles to Vesicles and Their Biological Applications. *Macromol. Rapid Commun.* **2009**, *30*, 267–277.

(9) Gröschel, A. H.; Müller, A. H. E. Self-Assembly Concepts for Multicompartment Nanostructures. *Nanoscale* **2015**, *7*, 11841–11876.

(10) Elsabahy, M.; Wooley, K. L. Design of Polymeric Nanoparticles for Biomedical Delivery Applications. *Chem. Soc. Rev.* **2012**, *41*, 2545–2561.

(11) Ge, Z.; Liu, S. Functional Block Copolymer Assemblies Responsive to Tumor and Intracellular Microenvironments for Site-Specific Drug Delivery and Enhanced Imaging Performance. *Chem. Soc. Rev.* **2013**, *42*, 7289.

(12) Lazzari, M.; Scalarone, D.; Vazquez-Vazquez, C.; López-Quintela, M. A. Cylindrical Micelles from the Self-Assembly of Polyacrylonitrile-Based Diblock Copolymers in Nonpolar Selective Solvents. *Macromol. Rapid Commun.* **2008**, *29*, 352–357.

(13) Du, Z. X.; Xu, J. T.; Fan, Z. Q. Micellar Morphologies of Poly(ε-caprolactone)-*b*-Poly(ethylene oxide) Block Copolymers in Water with a Crystalline Core. *Macromolecules* **2007**, *40*, 7633–7637.

(14) He, W. N.; Zhou, B.; Xu, J. T.; Du, B. Y.; Fan, Z. Q. Two Growth Modes of Semicrystalline Cylindrical Poly(ε-caprolactone)-*b*-Poly(ethylene oxide) Micelles. *Macromolecules* **2012**, *45*, 9768–9778.

(15) Zhang, J.; Wang, L. Q.; Wang, H.; Tu, K. Micellization Phenomena of Amphiphilic Block Copolymers Based on Methoxy Poly(ethylene glycol) and Either Crystalline or Amorphous Poly(caprolactone-*b*-lactide). *Biomacromolecules* **2006**, *7*, 2492–2500.

(16) Schmalz, H.; Schmelz, J.; Drechsler, M.; Yuan, J.; Walther, A.; Schweimer, K.; Mihut, A. M. Thermo-Reversible Formation of Wormlike Micelles with a Microphase-Separated Corona from a Semicrystalline Triblock Terpolymer. *Macromolecules* **2008**, *41*, 3235–3242.

(17) Yin, L.; Lodge, T. P.; Hillmyer, M. A. A Stepwise "Micellization-Crystallization" Route to Oblate Ellipsoidal, Cylindrical, and Bilayer Micelles with Polyethylene Cores in Water. *Macromolecules* **2012**, *45*, 9460–9467.

(18) Schmelz, J.; Karg, M.; Hellweg, T.; Schmalz, H. General Pathway toward Crystalline-Core Micelles with Tunable Morphology and Corona Segregation. *ACS Nano* **2011**, *5*, 9523–9534.

(19) Mihut, A. M.; Drechsler, M.; Möller, M.; Ballauff, M. Sphere-to-Rod Transition of Micelles Formed by the Semicrystalline Polybutadiene-Block-Poly(ethylene oxide) Block Copolymer in

a Selective Solvent. *Macromol. Rapid Commun.* **2010**, *31*, 449–453.

(20) Gilroy, J. B.; Lunn, D. J.; Patra, S. K.; Whittell, G. R.; Winnik, M. A.; Manners, I. Fiber-like Micelles *via* the Crystallization-Driven Solution Self-Assembly of poly(3-Hexylthiophene)-Block-Poly(methyl methacrylate) Copolymers. *Macromolecules* **2012**, *45*, 5806–5815.

(21) Massey, J. A.; Temple, K.; Cao, L.; Rharbi, Y.; Raez, J.; Winnik, M. A.; Manners, I. Self-Assembly of Organometallic Block Copolymers: The Role of Crystallinity of the Core-Forming Polyferrocene Block in the Micellar Morphologies Formed by Poly(ferrocenylsilane-*b*-dimethylsiloxane) in n-Alkane Solvents. *J. Am. Chem. Soc.* **2000**, *122*, 11577–11584.

(22) Kynaston, E. L.; Gould, O. E. C.; Gwyther, J.; Whittell, G. R.; Winnik, M. A.; Manners, I. Fiber-Like Micelles from the Crystallization-Driven Self-Assembly of Poly(3-Heptylselenophene)-Block-Polystyrene. *Macromol. Chem. Phys.* **2015**, *216*, 685–695.

(23) Legros, C.; De Pauw-Gillet, M.-C.; Tam, K. C.; Taton, D.; Lecommandoux, S. Crystallisation-Driven Self-Assembly of Poly(2-isopropyl-2-oxazoline)-Block-Poly(2-methyl-2-oxazoline) above the LCST. *Soft Matter* **2015**, *11*, 3354–3359.

(24) Yu, B.; Jiang, X.; Yin, J. Size-Tunable Nanosheets by the Crystallization-Driven 2D Self-Assembly of Hyperbranched Poly(ether amine) (hPEA). *Macromolecules* **2014**, *47*, 4761–4768.

(25) Tong, Z.; Li, Y.; Xu, H.; Chen, H.; Yu, W.; Zhuo, W.; Zhang, R.; Jiang, G. Corona Liquid Crystalline Order Helps to Form Single Crystals When Self-Assembly Takes Place in the Crystalline/Liquid Crystalline Block Copolymers. *ACS Macro Lett.* **2016**, *5*, 867–872.

(26) Wu, J.; Weng, L.-T.; Qin, W.; Liang, G.; Tang, B. Z. Crystallization-Induced Redox-Active Nanoribbons of Organometallic Polymers. *ACS Macro Lett.* **2015**, *4*, 593–597.

(27) Rizis, G.; van de Ven, T. G. M.; Eisenberg, A. Homopolymers as Structure-Driving Agents in Semicrystalline Block Copolymer Micelles. *ACS Nano* **2015**, *9*, 3627–3640.

(28) Lee, I.-H.; Amaladass, P.; Yoon, K.-Y.; Shin, S.; Kim, Y.-J.; Kim, I.; Lee, E.; Choi, T.-L. Nanostar and Nanonetwork Crystals Fabricated by *In Situ* Nanoparticlization of Fully Conjugated Polythiophene Diblock Copolymers. *J. Am. Chem. Soc.* **2013**, *135*, 17695–17698.

(29) Presa-Soto, D.; Carriedo, G. A.; de la Campa, R.; Presa Soto, A. Formation and Reversible Morphological Transition of Bicontinuous Nanospheres and Toroidal Micelles by the Self-Assembly of a Crystalline-*b*-Coil Diblock Copolymer. *Angew. Chem. Int. Ed.* **2016**, *55*, 10102–10107.

(30) Lee, C.-U.; Smart, T. P.; Guo, L.; Epps, T. H.; Zhang, D. Synthesis and Characterization of Amphiphilic Cyclic Diblock Copolypeptoids from N-Heterocyclic Carbene-Mediated Zwitterionic Polymerization of N-Substituted N-Carboxyanhydride. *Macromolecules* **2011**, *44*, 9574–9585.

(31) Yang, S.; Shin, S.; Choi, I.; Lee, J.; Choi, T.-L. Direct Formation of Large-Area 2D Nanosheets from Fluorescent Semiconducting Homopolymer with Orthorhombic Crystalline Orientation. *J. Am. Chem. Soc.* **2017**, *139*, 3082–3088.

(32) Tao, D.; Feng, C.; Cui, Y.; Yang, X.; Manners, I.; Winnik, M. A.; Huang, X. Monodisperse Fiber-like Micelles of Controlled Length and Composition with an Oligo(p-Phenylenevinylene) Core *via* "Living" Crystallization-Driven Self-Assembly. *J. Am. Chem. Soc.* **2017**, *139*, 7136–7139.

(33) Arno, M. C.; Inam, M.; Coe, Z.; Cambridge, G.; Macdougall, L. J.; Keogh, R.; Dove, A. P.; O'Reilly, R. K. Precision Epitaxy for Aqueous 1D and 2D Poly(ε-caprolactone) Assemblies. *J. Am. Chem. Soc.* **2017**, *139*, 16980–16985.

(34) Sun, L.; Pitto-Barry, A.; Kirby, N.; Schiller, T. L.; Sanchez, A. M.; Dyson, M. A.; Sloan, J.; Wilson, N. R.; O'Reilly, R. K.; Dove, A. P. Structural Reorganization of Cylindrical Nanoparticles Triggered by Polylactide Stereocomplexation. *Nat. Commun.* **2014**, *5*, 5746.

(35) Ganda, S.; Dulle, M.; Drechsler, M.; Förster, B.; Förster, S.; Stenzel, M. H. Two-Dimensional Self-Assembled Structures of Highly Ordered Bioactive Crystalline-Based Block Copolymers. *Macromolecules* **2017**, *50*, 8544–8553.

(36) Gilroy, J. B.; Gädt, T.; Whittell, G. R.; Chabanne, L.; Mitchels, J. M.; Richardson, R. M.; Winnik, M. A.; Manners, I. Monodisperse Cylindrical Micelles by Crystallization-Driven Living Self-Assembly. *Nat. Chem.* **2010**, *2*, 566–570.

(37) Hailes, R. L. N.; Oliver, A. M.; Gwyther, J.; Whittell, G. R.; Manners, I. Polyferrocenylsilanes: Synthesis, Properties, and Applications. *Chem. Soc. Rev.* **2016**, *45*, 5358–5407.

(38) Wang, X.; Guerin, G.; Wang, H.; Wang, Y.; Manners, I.; Winnik, M. A. Cylindrical Block Copolymer Micelles and Co-Micelles of Controlled Length and Architecture. *Science* **2007**, *317*, 644–647.

(39) Gädt, T.; Ieong, N. S.; Cambridge, G.; Winnik, M. A.; Manners, I. Complex and Hierarchical Micelle Architectures from Diblock Copolymers Using Living, Crystallization-Driven Polymerizations. *Nat. Mater.* **2009**, *8*, 144–150.

(40) Hudson, Z. M.; Lunn, D. J.; Winnik, M. A.; Manners, I. Colour-Tunable Fluorescent Multiblock Micelles. *Nat. Commun.* **2014**, *5*, 3372–3379.

(41) Finnegan, J. R.; Lunn, D. J.; Gould, O. E. C.; Hudson, Z. M.; Whittell, G. R.; Winnik, M. A.; Manners, I. Gradient Crystallization-Driven Self-Assembly: Cylindrical Micelles with "Patchy" Segmented Coronas *via* the Coassembly of Linear and Brush Block Copolymers. *J. Am. Chem. Soc.* **2014**, *136*, 13835–13844.

(42) Petzetakis, N.; Dove, A. P.; O'Reilly, R. K. Cylindrical Micelles from the Living Crystallization-Driven Self-Assembly of Poly(lactide)-Containing Block Copolymers. *Chem. Sci.* **2011**, *2*, 955–960.

(43) Schmelz, J.; Schedl, A. E.; Steinlein, C.; Manners, I.; Schmalz, H. Length Control and Block-Type Architectures in Worm-like Micelles with Polyethylene Cores. *J. Am. Chem. Soc.* **2012**, *134*, 14217–14225.

(44) Gwyther, J.; Gilroy, J. B.; Rupar, P. A.; Lunn, D. J.; Kynaston, E.; Patra, S. K.; Whittell, G. R.; Winnik, M. A.; Manners, I. Dimensional Control of Block Copolymer Nanofibers with a π-Conjugated Core: Crystallization-Driven Solution Self-Assembly of Amphiphilic Poly(3-Hexylthiophene)-B-poly(2-Vinylpyridine). *Chem. - Eur. J.* **2013**, *19*, 9186–9197.

(45) Ogi, S.; Stepanenko, V.; Sugiyasu, K.; Takeuchi, M.; Würthner, F. Mechanism of Self-Assembly Process and Seeded Supramolecular Polymerization of Perylene Bisimide Organogelator. *J. Am. Chem. Soc.* **2015**, *137*, 3300–3307.

(46) Zhang, W.; Jin, W.; Fukushima, T.; Saeki, A.; Seki, S.; Aida, T. Supramolecular Linear Heterojunction Composed of Graphite-Like Semiconducting Nanotubular Segments. *Science* **2011**, *334*, 340–343.

(47) Robinson, M. E.; Lunn, D. J.; Nazemi, A.; Whittell, G. R.; De Cola, L.; Manners, I. Length Control of Supramolecular Polymeric Nanofibers Based on Stacked Planar Platinum(II) Complexes by Seeded-Growth. *Chem. Commun.* **2015**, *51*, 15921–15924.

(48) Bu, L.; Dawson, T. J.; Hayward, R. C. Tailoring Ultrasound-Induced Growth of Perylene Diimide Nanowire Crystals from Solution by Modification with Poly(3-hexylthiophene). *ACS Nano* **2015**, *9*, 1878–1885.

(49) Ogi, S.; Sugiyasu, K.; Manna, S.; Samitsu, S.; Takeuchi, M. Living Supramolecular Polymerization Realized through a Biomimetic Approach. *Nat. Chem.* **2014**, *6*, 188–195.

(50) Pal, A.; Malakoutikhah, M.; Leonetti, G.; Tezcan, M.; Colomb-Delsuc, M.; Nguyen, V. D.; van der Gucht, J.; Otto, S. Controlling the Structure and Length of Self-Synthesizing Supramolecular Polymers through Nucleated Growth and Disassembly. *Angew. Chem. Int. Ed.* **2015**, *54*, 7852–7856.

(51) Ma, X.; Zhang, Y.; Zhang, Y.; Liu, Y.; Che, Y.; Zhao, J. Fabrication of Chiral-Selective Nanotubular Heterojunctions through Living Supramolecular Polymerization. *Angew. Chem. Int. Ed.* **2016**, *55*, 9539–9543.

(52) Fukui, T.; Kawai, S.; Fujinuma, S.; Matsushita, Y.; Yasuda, T.; Sakurai, T.; Seki, S.; Takeuchi, M.; Sugiyasu, K. Control over Differentiation of a Metastable Supramolecular Assembly in One and Two Dimensions. *Nat. Chem.* **2016**, *9*, 493–499.

(53) Greciano, E. E.; Sánchez, L. Seeded Supramolecular Polymerization in a Three-Domain Self-Assembly of an N-Annulated Perylenetetracarboxamide. *Chem. - Eur. J.* **2016**, *22*, 13724–13730.

(54) He, X.; Hsiao, M.-S.; Boott, C. E.; Harniman, R. L.; Nazemi, A.; Li, X.; Winnik, M. A.; Manners, I. Two-Dimensional Assemblies from Crystallizable Homopolymers with Charged Termini. *Nat. Mater.* **2017**, *16*, 481–488.

(55) Görl, D.; Zhang, X.; Stepanenko, V.; Würthner, F. Supramolecular Block Copolymers by Kinetically Controlled Co-Self-Assembly of Planar and Core-Twisted Perylene Bisimides. *Nat. Commun.* **2015**, *6*, 7009.

(56) Zhang, W.; Jin, W.; Fukushima, T.; Mori, T.; Aida, T. Helix Sense-Selective Supramolecular Polymerization Seeded by a One-Handed Helical Polymeric Assembly. *J. Am. Chem. Soc.* **2015**, *137*, 13792–13795.

(57) Boott, C. E.; Gwyther, J.; Harniman, R. L.; Hayward, D. W.; Manners, I. Scalable and Uniform 1D Nanoparticles by Synchronous Polymerization, Crystallization and Self-Assembly. *Nat. Chem.* **2017**, *9*, 785–792.

(58) Hudson, Z. M.; Boott, C. E.; Robinson, M. E.; Rupar, P. A.; Winnik, M. A.; Manners, I. Tailored Hierarchical Micelle Architectures Using Living Crystallization-Driven Self-Assembly in Two Dimensions. *Nat. Chem.* **2014**, *6*, 893–898.

(59) Qiu, H.; Gao, Y.; Boott, C. E.; Gould, O. E. C.; Harniman, R. L.; Miles, M. J.; Webb, S. E. D.; Winnik, M. A.; Manners, I. Uniform Patchy and Hollow Rectangular Platelet Micelles from Crystallizable Polymer Blends. *Science* **2016**, *352*, 697–701.

(60) Rupar, P. A.; Chabanne, L.; Winnik, M. A.; Manners, I. Non-Centrosymmetric Cylindrical Micelles by Unidirectional Growth. *Science* **2012**, *337*, 559–562.

(61) Qiu, H.; Du, V. A.; Winnik, M. A.; Manners, I. Branched Cylindrical Micelles *via* Crystallization-Driven Self-Assembly. *J. Am. Chem. Soc.* **2013**, *135*, 17739–17742.

(62) Qiu, H.; Cambridge, G.; Winnik, M. A.; Manners, I. Multi-Armed Micelles and Block Co-Micelles *via* Crystallization-Driven Self-Assembly with Homopolymer Nanocrystals as Initiators. *J. Am. Chem. Soc.* **2013**, *135*, 12180–12183.

(63) Qiu, H.; Russo, G.; Rupar, P. A.; Chabanne, L.; Winnik, M. A.; Manners, I. Tunable Supermicelle Architectures from the Hierarchical Self-Assembly of Amphiphilic Cylindrical B-A-B Triblock Co-Micelles. *Angew. Chem. Int. Ed.* **2012**, *51*, 11882–11885.

(64) Qiu, H.; Hudson, Z. M.; Winnik, M. A.; Manners, I. Multidimensional Hierarchical Self-Assembly of Amphiphilic Cylindrical Block Comicelles. *Science* **2015**, *347*, 1329–1332.

(65) Gilroy, J. B.; Rupar, P. A.; Whittell, G. R.; Chabanne, L.; Terrill, N. J.; Winnik, M. A.; Manners, I.; Richardson, R. M. Probing the Structure of the Crystalline Core of Field-Aligned, Monodisperse, Cylindrical Polyisoprene- Block -Polyferrocenylsilane Micelles in Solution Using Synchrotron Small- and Wide-Angle X-Ray Scattering. *J. Am. Chem. Soc.* **2011**, *133*, 17056–17062.

(66) Hsiao, M.-S.; Yusoff, S. F. M.; Winnik, M. A.; Manners, I. Crystallization-Driven Self-Assembly of Block Copolymers with a Short Crystallizable Core-Forming Segment: Controlling Micelle Morphology through the Influence of Molar Mass and Solvent Selectivity. *Macromolecules* **2014**, *47*, 2361–2372.

(67) Nazemi, A.; He, X.; MacFarlane, L. R.; Harniman, R. L.; Hsiao, M.-S.; Winnik, M. A.; Faul, C. F. J.; Manners, I. Uniform “Patchy” Platelets by Seeded Heteroepitaxial Growth of Crystallizable Polymer Blends in Two Dimensions. *J. Am. Chem. Soc.* **2017**, *139*, 4409–4417.

(68) Gustafsson, M. G. L.; Shao, L.; Carlton, P. M.; Wang, C. J. R.; Golubovskaya, I. N.; Cande, W. Z.; Agard, D. A.; Sedat, J. W. Three-Dimensional Resolution Doubling in Wide-Field Fluorescence Microscopy by Structured Illumination. *Biophys. J.* **2008**, *94*, 4957–4970.

(69) Ströhl, F.; Kaminski, C. F. Frontiers in Structured Illumination Microscopy. *Optica* **2016**, *3*, 667.

(70) Hell, S. W.; Wichmann, J. Breaking the Diffraction Resolution Limit by Stimulated Emission: Stimulated-Emission-Depletion Fluorescence Microscopy. *Opt. Lett.* **1994**, *19*, 780–782.

(71) Klar, T. A.; Jakobs, S.; Dyba, M.; Egner, A.; Hell, S. W. Fluorescence Microscopy with Diffraction Resolution Barrier Broken by Stimulated Emission. *Proc. Natl. Acad. Sci. U.S.A.* **2000**, *97*, 8206–8210.

(72) Nespovitaya, N.; Mahou, P.; Laine, R. F.; Schierle, G. S. K.; Kaminski, C. F. Heparin Acts as a Structural Component of β-Endorphin Amyloid Fibrils rather than a Simple Aggregation Promoter. *Chem. Commun.* **2017**, *53*, 1273–1276.

(73) Rust, M. J.; Bates, M.; Zhuang, X. Sub-Diffraction-Limit Imaging by Stochastic Optical Reconstruction Microscopy (STORM). *Nat. Methods* **2006**, *3*, 793–795.

(74) Hess Girirajan T, Mason M, S. Ultra-High Resoluion Imaging by Fluorescence Photoactivation Localization Microscopy. *Biophys. J.* **2006**, *91*, 4258–4272.

(75) Betzig, E.; Patterson, G. H.; Sougrat, R.; Lindwasser, O. W.; Olenych, S.; Bonifacino, J. S.; Davidson, M. W.; Lippincott-Schwartz, J.; Hess, H. F. Imaging Intracellular Fluorescent Proteins at Nanometer Resolution. *Science* **2006**, *313*, 1642–1645.

(76) Heilemann, M.; Van De Linde, S.; Schüttpelz, M.; Kasper, R.; Seefeldt, B.; Mukherjee, A.; Tinnefeld, P.; Sauer, M. Subdiffraction-Resolution Fluorescence Imaging with Conventional Fluorescent Probes. *Angew. Chem. Int. Ed.* **2008**, *47*, 6172–6176.

(77) Huang, B.; Wang, W.; Bates, M.; Zhuang, X. Three-Dimensional Super-Resolution Imaging by Stochastic Optical Reconstruction Microscopy. *Science* **2008**, *319*, 810–813.

(78) Pinotsi, D.; Buell, A. K.; Galvagnion, C.; Dobson, C. M.; Kaminski Schierle, G. S.; Kaminski, C. F. Direct Observation of Heterogeneous Amyloid Fibril Growth Kinetics *via* Two-Color Super-Resolution Microscopy. *Nano Lett.* **2014**, *14*, 339–345.

(79) Kaminski Schierle, G. S.; Van De Linde, S.; Erdelyi, M.; Esbjörner, E. K.; Klein, T.; Rees, E.; Bertoncini, C. W.; Dobson, C. M.; Sauer, M.; Kaminski, C. F. *In Situ* Measurements of the Formation and Morphology of Intracellular β-Amyloid Fibrils by Super-Resolution Fluorescence Imaging. *J. Am. Chem. Soc.* **2011**, *133*, 12902–12905.

(80) Roberti, M. J.; Fölling, J.; Celej, M. S.; Bossi, M.; Jovin, T. M.; Jares-Erijman, E. A. Imaging Nanometer-Sized α-Synuclein Aggregates by Superresolution Fluorescence Localization Microscopy. *Biophys. J.* **2012**, *102*, 1598–1607.

(81) Duim, W. C.; Chen, B.; Frydman, J.; Moerner, W. E. Sub-Diffraction Imaging of Huntingtin Protein Aggregates by Fluorescence Blink-Microscopy and Atomic Force Microscopy. *ChemPhysChem* **2011**, *12*, 2387–2390.

(82) Ries, J.; Udayar, V.; Soragni, A.; Hornemann, S.; Nilsson, K. P. R.; Riek, R.; Hock, C.; Ewers, H.; Aguzzi, A. A.; Rajendran, L. Superresolution Imaging of Amyloid Fibrils with Binding-Activated Probes. *ACS Chem. Neurosci.* **2013**, *4*, 1057–1061.

(83) Kaminski, C. F.; Kaminski Schierle, G. S. Probing Amyloid Protein Aggregation with Optical Superresolution Methods: From the Test Tube to Models of Disease. *Neurophotonics* **2016**, *3*, 41807.

(84) Gaspar, R.; Meisl, G.; Buell, A. K.; Young, L.; Kaminski, C. F.; Knowles, T. P. J.; Sparr, E.;

Linse, S. Secondary Nucleation of Monomers on Fibril Surface Dominates α-Synuclein Aggregation and Provides Autocatalytic Amyloid Amplification. *Q. Rev. Biophys.* **2017**, *50*, e6.

(85) Albertazzi, L.; van der Zwaag, D.; Leenders, C. M. A.; Fitzner, R.; van der Hofstad, R. W.; Meijer, E. W. Probing Exchange Pathways in One-Dimensional Aggregates with Super-Resolution Microscopy. *Science* **2014**, *344*, 491–495.

(86) Adelizzi, B.; Aloi, A.; Van Zee, N. J.; Palmans, A. R. A.; Meijer E. W.; Voets, I. K. Painting Supramolecular Polymers in Organic Solvents by Super-resolution Microscopy *ACS Nano* **2018**, *12*, 4431–4439.

(87) Boott, C. E.; Laine, R. F.; Mahou, P.; Finnegan, J. R.; Leitao, E. M.; Webb, S. E. D.; Kaminski, C. F.; Manners, I. *In Situ* Visualization of Block Copolymer Self-Assembly in Organic Media by Super-Resolution Fluorescence Microscopy. *Chem. - Eur. J.* **2015**, *21*, 18539–18542.

(88) Ni, Y.; Rulkens, R.; Manners, I. Transition Metal-Based Polymers with Controlled Architectures: Well-Defined Poly(ferrocenylsilane) Homopolymers and Multiblock Copolymers *via* the Living Anionic Ring-Opening Polymerization of Silicon-Bridged [1]Ferrocenophanes. *J. Am. Chem. Soc.* **1996**, *118*, 4102–4114.

(89) Hayward, D. W.; Gilroy, J. B.; Rupar, P. A.; Chabanne, L.; Pizzey, C.; Winnik, M. A.; Whittell, G. R.; Manners, I.; Richardson, R. M. Liquid Crystalline Phase Behavior of Well-Defined Cylindrical Block Copolymer Micelles Using Synchrotron Small-Angle X-Ray Scattering. *Macromolecules* **2015**, *48*, 1579–1591.

(90) Qiu, H.; Gao, Y.; Du, V. A.; Harniman, R.; Winnik, M. A.; Manners, I. Branched Micelles by Living Crystallization-Driven Block Copolymer Self-Assembly under Kinetic Control. *J. Am. Chem. Soc.* **2015**, *137*, 2375–2385.

(91) The linear aggregation number can also be determined by static light scattering. Using this method a linear aggregation number of 2.5 chain/nm was also obtained for the comparable BCP, PFS_{50}-*b*-$PDMS_{285}$. Cambridge, G.; Guerin, G.; Manners, I.; Winnik, M. A. Fiberlike Micelles Formed by Living Epitaxial Growth from Blends of Polyferrocenylsilane Block Copolymers. *Macromol. Rapid Commun.* **2010**, *31*, 934–938.

(92) Odian, G. *Principles of Polymerization*, 4th ed.; John Wiley and Sons, 2004.

(93) Sanchez, I. C.; Colson, J. P.; Eby, R. K. Theory and Observations of Polymer Crystal Thickening. *J. Appl. Phys.* **1973**, *44*, 4332–4339.

(94) Doye, J. The Effect of Temperature Jumps during Polymer Crystallization. *Polymer* **2000**, *41*, 1519–1528.

(95) Barton, A. F. M. *CRC Handbook of Solubility Parameters and Other Cohesion Parameters*, Second.; CRC Press, 1991.

(96) Kulbaba, K.; MacLachlan, M. J.; Evans, C. E. B.; Manners, I. Organometallic Gels: Characterization and Electrochemical Studies of Swellable, Thermally Crosslinked Poly(ferrocenylsilane)s. *Macromol. Chem. Phys.* **2001**, *202*, 1768–1775.

(97) Zhou, Y.; Hu, W. Kinetic Analysis of Quasi-One-Dimensional Growth of Polymer Lamellar Crystals in Dilute Solutions. *J. Phys. Chem. B* **2013**, *117*, 3047–3053.

(98) Xu, J.; Ma, Y.; Hu, W.; Rehahn, M.; Reiter, G. Cloning Polymer Single Crystals through Self-Seeding. *Nat. Mater.* **2009**, *8*, 348–353.

(99) Guerin, G.; Rupar, P.; Molev, G.; Manners, I.; Jinnai, H.; Winnik, M. A. Lateral Growth of 1D Core-Crystalline Micelles upon Annealing in Solution. *Macromolecules* **2016**, *49*, 7004–7014.

(100) The height by AFM of the seed micelles is significantly less than that for the parent micelles (See Ref. 13, Figure S2 and S1, respectively). This suggests that some structural reorganization of the micelle occurs after prolonged ultrasound, but without any reduction in

the fidelity of the seed for further growth.

(101) McDonough, R.; Cueto, R.; Phillies, G. D. J.; Russo, P. S.; Dorman, D.; Streletzky, K. A. Fluorescent Labeling Can Alter Polymer Solution Dynamics. *Macromolecules* **2015**, *48*, 7245–7255.

(102) Mahou, P.; Curry, N.; Pinotsi, D.; Kaminski Schierle, G.; Kaminski, C. Stimulated Emission Depletion Microscopy to Study Amyloid Fibril Formation; Enderlein, J., Gregor, I., Gryczynski, Z. K., Erdmann, R., Koberling, F., Eds.; 2015; p 93310U.

TOC Image: